INTERNATIONAL JOURNAL FOR NUMERICAL METHODS IN FLUIDS, VOL. 7, 1325–1342 (1987)

FINITE-ELEMENT ANALYSIS OF FLUID FLOW AND HEAT TRANSFER FOR STAGGERED BUNDLES OF CYLINDERS IN CROSS FLOW

M. N. DHAUBHADEL, J. N. REDDY AND D. P. TELIONIS

Department of Engineering Science and Mechanics, Virginia Polytechnic Institute and State University, Blacksburg, Virginia 24061, U.S.A.

SUMMARY

The two-dimensional Navier–Stokes equations and the energy equation governing steady laminar incompressible flow are solved by a penalty finite-element model for flow across finite depth, five-row deep, staggered bundles of cylinders. Pitch to diameter ratios of 1·5 and 2·0 are considered for cylinders in equilateral triangular and square arrangements. Reynolds numbers studied range from 100 to 400, and a Prandtl number of 0·7 is used. Velocity vector fields, streamline patterns, vorticity, pressure and temperature contours, local and average Nusselt numbers, pressure and shear stress distributions around the cylinder walls and drag coefficients are presented. The results obtained agree well with available experimental and numerical data.

KEY WORDS Convective Heat Transfer Finite Elements Navier–Stokes Equations Numerical Results Penalty Model Staggered Cylinders

INTRODUCTION

The hydrodynamic and heat transfer characteristics of fluid flow around cylinders are of interest in the design of heat exchangers, boilers, condensers, nuclear reactors, etc. Investigations on the flow and heat transfer for a bundle of cylinders in cross-flow have been undertaken by numerous researchers. Experimental data on fluid mechanics and heat transfer of flow around staggered cylinders have been presented by Zukauskas,[1] Aiba *et al.*,[2] Kostic and Oka[3] and Bergelin *et al.*[4,5] Experimental data on the effect of pulsation of the free stream on flow and heat transfer characteristics for multiple cylinders have been presented by Vanden Berghe *et al.*[6] Numerical studies using finite-difference methods for fluid flow and heat transfer across multiple cylinders have appeared recently. LeFeuvre[7] obtained a finite-difference solution for an in-line bank with uniform tube wall temperature. Launder and Massey[8] obtained a finite-difference solution for the inner row of a staggered tube bank with the assumption of uniform wall heat flux. Fujii *et al.*[9] used the one-step-forward half-step-backward iteration hybrid finite-difference method to solve the stream function–vorticity and energy equations for a five-row in-line tube bank. Antonopoulos[10] used the finite-difference method to solve the transport equations in curvilinear co-ordinates for turbulent inclined flow past an interior region of a tube bank. The present paper offers penalty finite-element solutions to the problems of flow across staggered bundles of cylinders, with uniform wall temperature.

The problem under consideration here offers physical insight into the development of the flow and the accompanied heat transfer characteristics as we move deeper into the bundle. In this sense,

0271-2091/87/121325-18$09.00

Received 5 May 1986
Revised 21 January 1987

therefore, this paper extends the work of Fujii *et al.*[9] to bundle geometries more common in practice, employing a powerful numerical method which so far has not been used for the solution of such problems.

The finite-element method allows suitable representation of the complicated geometry of multiple cylinders without having to use curvilinear co-ordinates or mapping. Moreover, flux and stress boundary conditions of the flow can be imposed in a natural way without requiring difference approximations. Finite-element simulations of flow past a single cylinder have been presented by Kawahara and Hirano,[11] Gresho *et al.*,[12] Brooks and Hughes[13] and Benque *et al.*[14] A penalty finite-element solution for flow and heat transfer around in-line bundles of cylinders was recently obtained by the authors.[15]

This paper presents a penalty finite-element model to solve the Navier–Stokes equations and the energy equation as applied to laminar incompressible flow across a staggered bundle of cylinders. Five-row-deep bundles of cylinders in two equilateral triangular arrangements and a square arrangement are studied. Pitch to diameter ratios of 1·5 and 2·0 are considered. Reynolds numbers studied range from 100 to 400, and the Prandtl number is assumed to be 0·7.

THEORETICAL CONSIDERATIONS AND THE PENALTY FINITE-ELEMENT MODEL

For two-dimensional laminar flow of an incompressible fluid with negligible viscous dissipation, the Navier–Stokes equations and the energy equation in non-dimensional form can be written as

$$u\frac{\partial u}{\partial x}+v\frac{\partial u}{\partial y}=\frac{2}{Re}\frac{\partial^2 u}{\partial x^2}+\frac{1}{Re}\frac{\partial}{\partial y}\left(\frac{\partial u}{\partial y}+\frac{\partial v}{\partial x}\right)-\frac{\partial p}{\partial x}+f_x, \tag{1}$$

$$u\frac{\partial v}{\partial x}+v\frac{\partial v}{\partial y}=\frac{1}{Re}\frac{\partial}{\partial x}\left(\frac{\partial u}{\partial y}+\frac{\partial v}{\partial x}\right)+\frac{2}{Re}\frac{\partial^2 v}{\partial y^2}-\frac{\partial p}{\partial y}+f_y, \tag{2}$$

$$\frac{\partial u}{\partial x}+\frac{\partial v}{\partial y}=0, \tag{3}$$

$$u\frac{\partial \theta}{\partial x}+v\frac{\partial \theta}{\partial y}=\frac{1}{Re\,Pr}\left(\frac{\partial^2 \theta}{\partial x^2}+\frac{\partial^2 \theta}{\partial y^2}\right), \tag{4}$$

where (u, v), $p, (f_x, f_y)$, θ are the non-dimensional velocity components, pressure, body force components and temperature, respectively, Re denotes the Reynolds number and Pr denotes the Prandtl number.

The penalty function formulation of equations (1)–(3) over a typical element Ω^e with boundary Γ^e is given by (see References 16–19 for details on the penalty function formulation)

$$\begin{aligned}0=&\int_{\Omega^e}\left[w_1\left(u\frac{\partial u}{\partial x}+v\frac{\partial u}{\partial y}\right)+\frac{2}{Re}\frac{\partial w_1}{\partial x}+\frac{\partial u}{\partial x}+\frac{1}{Re}\frac{\partial w_1}{\partial y}\left(\frac{\partial u}{\partial y}+\frac{\partial v}{\partial x}\right)-w_1 f_x\right]\mathrm{d}x\,\mathrm{d}y\\&+\int_{\Omega^e}\gamma\frac{\partial w_1}{\partial x}\left(\frac{\partial u}{\partial x}+\frac{\partial v}{\partial y}\right)\mathrm{d}x\,\mathrm{d}y-\int_{\Gamma^e}w_1\left[\left(\frac{2}{Re}\frac{\partial u}{\partial x}-p\right)n_x+\frac{1}{Re}\left(\frac{\partial u}{\partial y}+\frac{\partial v}{\partial x}\right)n_y\right]\mathrm{d}s,\end{aligned} \tag{5}$$

$$\begin{aligned}0=&\int_{\Omega^e}\left[w_2\left(u\frac{\partial v}{\partial x}+v\frac{\partial v}{\partial y}\right)+\frac{1}{Re}\frac{\partial w_2}{\partial x}\left(\frac{\partial u}{\partial y}+\frac{\partial v}{\partial x}\right)+\frac{2}{Re}\frac{\partial w_2}{\partial y}\frac{\partial v}{\partial y}-w_2 f_y\right]\mathrm{d}x\,\mathrm{d}y\\&+\int_{\Omega^e}\gamma\frac{\partial w_2}{\partial y}\left(\frac{\partial u}{\partial x}\right)\mathrm{d}x\,\mathrm{d}y-\int_{\Gamma^e}w_2\left[\frac{1}{Re}\left(\frac{\partial u}{\partial y}+\frac{\partial v}{\partial x}\right)n_x+\left(\frac{2}{Re}\frac{\partial v}{\partial y}-p\right)n_y\right]\mathrm{d}s,\end{aligned} \tag{6}$$

where w_1 and w_2 are the weight functions associated with u and v, respectively, γ is the penalty parameter, and n_x and n_y are direction cosines. The coefficients of w_1 and w_2 in the boundary integrals of equations (5) and (6) are denoted by t_x and t_y, respectively. They represent the x- and y-components of the boundary stress vector. The body force terms in equations (5) and (6) are neglected. The variational formulation of energy (4) is given by

$$0=\int_{\Omega^e}\left[w_3\left(u\frac{\partial\theta}{\partial x}+v\frac{\partial\theta}{\partial y}\right)+\frac{1}{Re\,Pr}\left(\frac{\partial w_3}{\partial x}\frac{\partial\theta}{\partial x}+\frac{\partial w_3}{\partial y}\frac{\partial\theta}{\partial y}\right)\right]\mathrm{d}x\,\mathrm{d}y-\int_{\Gamma^e}w_3\left(\frac{\partial\theta}{\partial x}n_x+\frac{\partial\theta}{\partial y}n_y\right)\mathrm{d}s, \tag{7}$$

where w_3 denotes the weight function associated with θ. The coefficient of w_3 in the boundary integral of equation (7) is denoted by t_θ, which denotes the non-dimensionalized boundary heat flux. Temperature is viewed as an inert scalar quantity transported and diffused according to the velocity field.

Let the dependent variables u, v and θ be interpolated over a typical element by expressions of the form

$$u=\sum_{j=1}^{n}u_j\psi_j,\quad v=\sum_{j=1}^{n}v_j\psi_j,\quad \theta=\sum_{j=1}^{n}\theta_j\psi_j, \tag{8}$$

where ψ_j are the finite-element interpolation functions,[19,20] u_j, v_j and θ_j are the nodal values of u, v and θ, respectively, and n denotes the number of nodes in the element.

Substituting equation (8) into equations (5)–(7), we obtain the ith element equations associated with equations (5)–(7)

$$\sum_{j=1}^{n}\bar{K}_{ij}^{11}u_j+\sum_{j=1}^{n}\bar{K}_{ij}^{12}v_j-F_i^1=0, \tag{9}$$

$$\sum_{j=1}^{n}\bar{K}_{ij}^{21}u_j+\sum_{j=1}^{n}\bar{K}_{ij}^{22}v_j-F_i^2=0, \tag{10}$$

$$\sum_{j=1}^{n}\bar{K}_{ij}^{1}\theta_j-F_i^\theta=0. \tag{11}$$

These equations can be written in matrix form as

$$\begin{bmatrix}[\bar{\mathbf{K}}^{11}] & [\bar{\mathbf{K}}^{12}]\\ [\bar{\mathbf{K}}^{12}] & [\bar{\mathbf{K}}^{22}]\end{bmatrix}\begin{Bmatrix}\{\mathbf{u}\}\\ \{\mathbf{v}\}\end{Bmatrix}=\begin{Bmatrix}\{\mathbf{F}^1\}\\ \{\mathbf{F}^2\}\end{Bmatrix}, \tag{12}$$

$$[\mathbf{K}^1]\{\boldsymbol{\theta}\}=\{\mathbf{F}^{\theta}\}, \tag{13}$$

where

$$[\bar{\mathbf{K}}^{11}]=[\mathbf{K}^{11}]+[\mathbf{G}]+\gamma[\mathbf{S}^{11}],$$

$$[\bar{\mathbf{K}}^{12}]=[\mathbf{K}^{12}]+\gamma[\mathbf{S}^{12}],$$

$$[\bar{\mathbf{K}}^{21}]=[\mathbf{K}^{21}]+\gamma[\mathbf{S}^{21}],$$

$$[\bar{\mathbf{K}}^{22}]=[\mathbf{K}^{22}]+[\mathbf{G}]+\gamma[\mathbf{S}^{22}],$$

$$[\mathbf{K}^{11}]=\frac{2}{Re}[S^{11}]+\frac{1}{Re}[\mathbf{S}^{22}],$$

$$[\mathbf{K}^{12}]=[\mathbf{K}^{21}]^{\mathrm{T}}=\frac{1}{Re}[\mathbf{S}^{12}]^{\mathrm{T}},$$

$$[\mathbf{K}^{22}]=[\mathbf{S}^{11}]=\frac{2}{Re}[\mathbf{S}^{22}],$$

$$[\mathbf{K}^1] = \frac{1}{Re\,Pr}\{[\mathbf{S}^{11}] + [\mathbf{S}^{22}]\} + [\mathbf{G}].$$

The coefficient matrices in the above equations are given by the following integral expressions:

$$\begin{aligned}
G_{ij} &= \int_{\Omega^e} \psi_i\left(u_0\frac{\partial\psi_j}{\partial x} + v_0\frac{\partial\psi_j}{\partial y}\right)\mathrm{d}x\,\mathrm{d}y,\\
S_{ij}^{11} &= \int_{\Omega^e} \frac{\partial\psi_i}{\partial x}\frac{\partial\psi_j}{\partial x}\mathrm{d}x\,\mathrm{d}y,\\
S_{ij}^{22} &= \int_{\Omega^e} \frac{\partial\psi_i}{\partial y}\frac{\partial\psi_j}{\partial y}\mathrm{d}x\,\mathrm{d}y,\\
S_{ij}^{12} &= \int_{\Omega^e} \frac{\partial\psi_i}{\partial x}\frac{\partial\psi_j}{\partial y}\mathrm{d}x\,\mathrm{d}y,\\
F_i^1 &= \int_{\Omega^e} f_x\psi_i\,\mathrm{d}x\,\mathrm{d}y + \int_{\Gamma^e} t_x\psi_i\,\mathrm{d}s,\\
F_i^2 &= \int_{\Omega^e} f_y\psi_i\,\mathrm{d}x\,\mathrm{d}y + \int_{\Gamma^e} t_y\psi_i\,\mathrm{d}s,\\
F_i^\theta &= \int_{\Omega^e} \psi_i t_\theta\,\mathrm{d}s,
\end{aligned} \tag{14}$$

where u_0 and v_0 are velocities from a previous iteration.

From convergence and stability considerations,[19] a reduced integration technique is used to evaluate the penalty terms (i.e. coefficients of γ in equation (12)). For the bilinear element ($n = 4$) employed in the present study, a 2 × 2 Gauss quadrature is used to evaluate all coefficients except the penalty terms, for which 1 × 1 quadrature is employed. Because of the presence of non-linear (convective) terms, the coefficient matrices for the Navier–Stokes equations are asymmetric, and an iterative solution is required. In the present study the direct (Picard type) iteration is used with initially zero velocity everywhere inside the computational domain, and convergence is assumed when the Euclidean norm of the velocities computed at two consecutive iterations is less than an error tolerance of 0·01 per cent. The energy equation (13) is solved using the velocity field obtained from equation (12). The secondary quantities, namely the pressure and the gradients of velocity and temperature, are computed at Gauss points. In the penalty function formulation the negative of pressure acts as a Lagrange parameter and the pressure is evaluated in post-computation by

$$P_n = -\gamma\left(\frac{\partial u}{\partial x} + \frac{\partial v_n}{\partial y}\right),$$

where the subscript n indicates values computed from the converged velocity field.

DISCUSSION OF THE NUMERICAL RESULTS

The physical models of flow around five-row-deep (finite) staggered bundles of cylinders in three different configurations are shown in Figures 1(a), 1(b) and 1(c). The computational domain is shown by the thick dotted line in Figure 1(a). For relatively low Reynolds numbers and closely packed cylinders, it is reasonable to assume that the wake of each cylinder is symmetric. In fact, no shedding occurs, even for relatively high Reynolds numbers, if the cylinders are tightly packed. It is

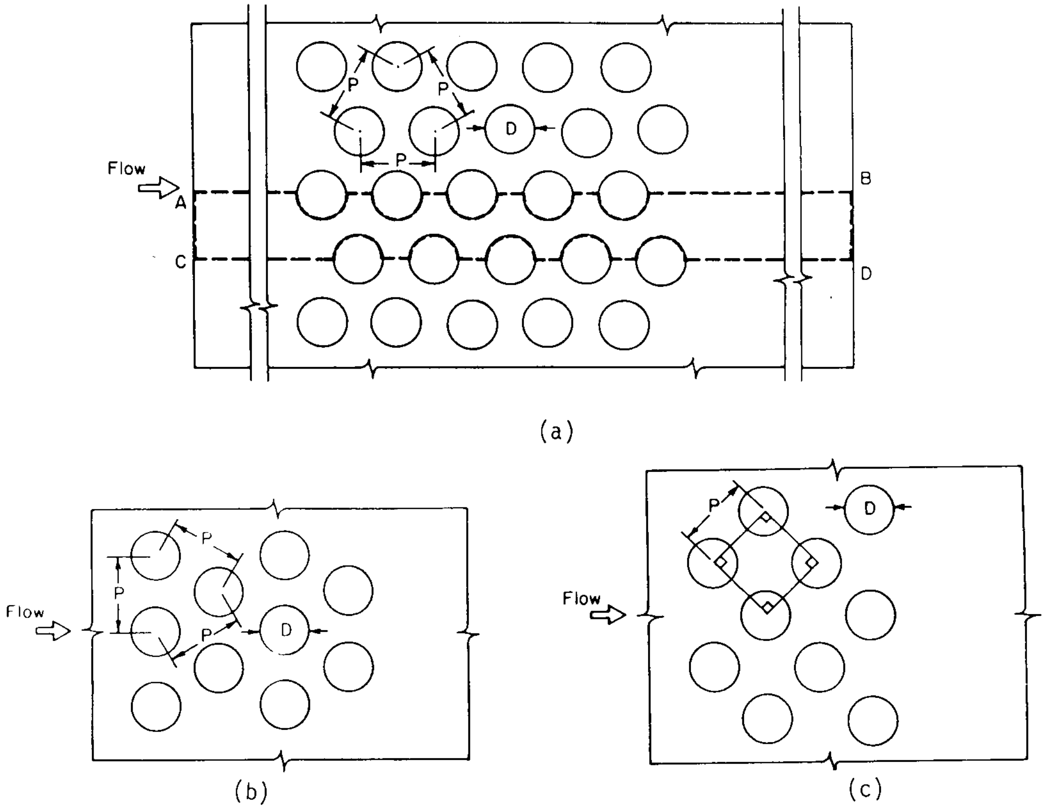

Figure 1. Physical model and computational domain of a five-row deep staggered bundle of cylinders: (a) cylinders in equilateral arrangement; (b) cylinders in equilateral arrangement turned at 90° with respect to free stream as compared to (a); (c) cylinders in staggered square arrangement

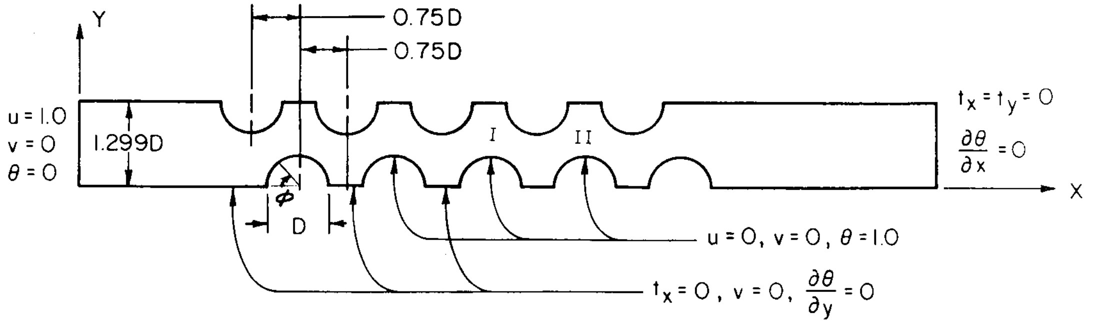

Figure 2. Boundary conditions

assumed here that the flow is steady, and symmetry lines exist as depicted in Figure 2. The boundary conditions employed in the present computations are also indicated in this Figure. Figure 3 shows a typical finite element mesh used. The nodal co-ordinates and the connectivity matrix, including the boundary conditions, are generated with the computer program for any number of rows in a bundle with the minimum of input parameters. The finite element mesh is designed in a way which provides a denser mesh in the boundary layers and along the free shear

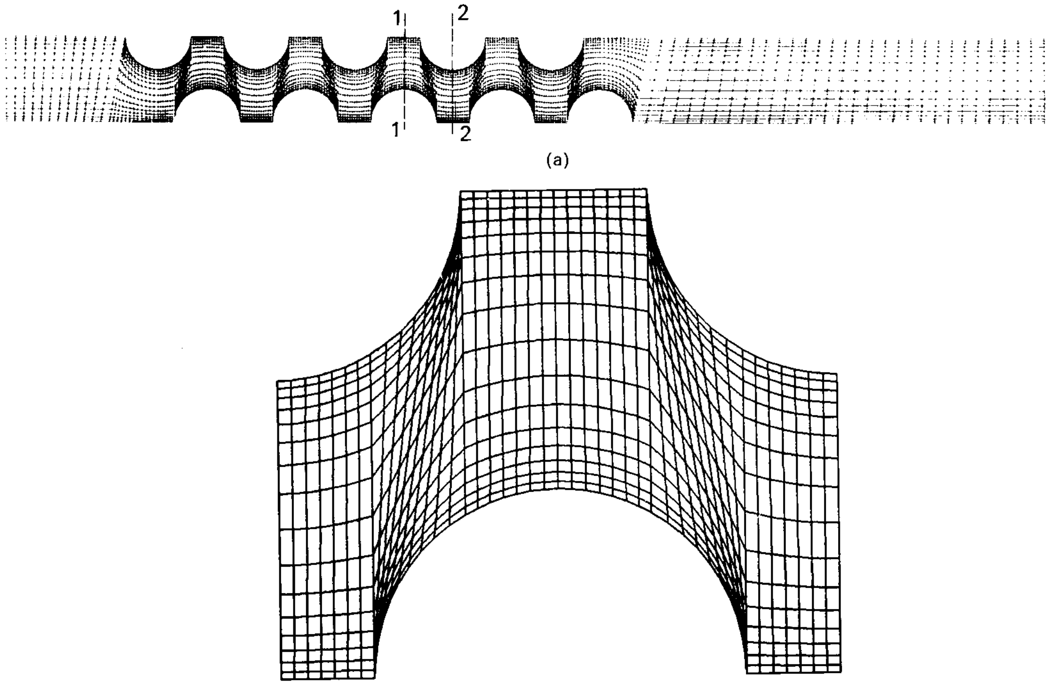

(a)

(b)

Figure 3(a). Finite element mesh with 4811 nodes and 4512 elements. (b) Detail of the finite element mesh

layers. For the Reynolds numbers considered, approximately 5 to 6 grid points fall within the boundary layer. This ensures reasonable resolution of boundary-layer effects near cylinder walls. The thickness of an element increases in geometrical proportion away from the cylinder surface. Two different finite-element meshes were used in the computations in order to ascertain that the discretization error is reduced to an acceptable level. Also, two different sets of inlet and outlet straight portions were used to consider the effects of the upstream and downstream boundary locations. Figure 3(a) shows the finite element mesh used with 4811 nodes and 4512 elements. The other mesh employed has a similar finite element discretization with slightly different inlet and outlet boundary locations and with a total of 3679 nodes and 3384 elements. The results obtained in terms of different fluid dynamic quantities discussed later indicate that the discretization error and the effect of inlet and outlet boundary locations are minimized to acceptable levels for the two mesh configurations used. The computations were carried out on a CRAY-XMP computer. A typical run for $Re = 100$ takes 190 s (CPU + I/0) and 20 iterations for convergence.

Figure 4(a) shows a typical velocity vector field obtained for an equilateral triangular arrangement with pitch to diameter ratio of 1·5 and a Reynolds number of 100 based on velocity at the minimum cross-section. The velocity profiles at sections 1–1 and 2–2 (see Figure 3(a)) for the two mesh configurations are plotted for comparison and are shown in Figure 4(b). The differences in the velocity profiles at the two sections are small, indicating that the discretization error is negligible for the two mesh configurations used. Figures 3(a) and 4(a) indicate that the velocity field after the third cylinder is almost fully developed. The difference in velocity field between regions I and II in Figure 2 is 0·75 per cent. The flow field in each of the three configurations is similar for different Reynolds numbers in the range studied. For a Reynolds number of 100

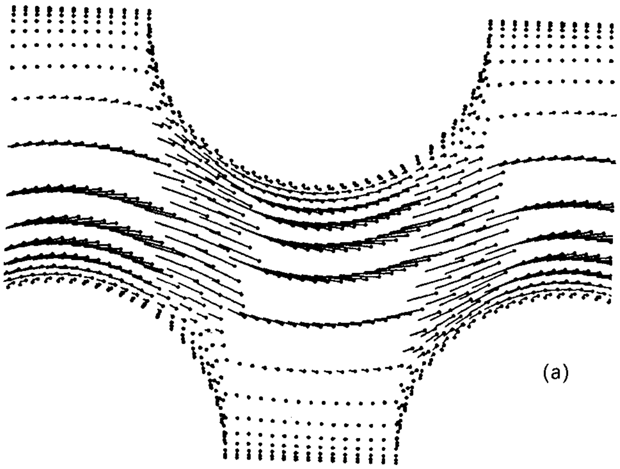

Figure 4(a). Enlarged view of velocity vectors in the region between I and II in Figure 2

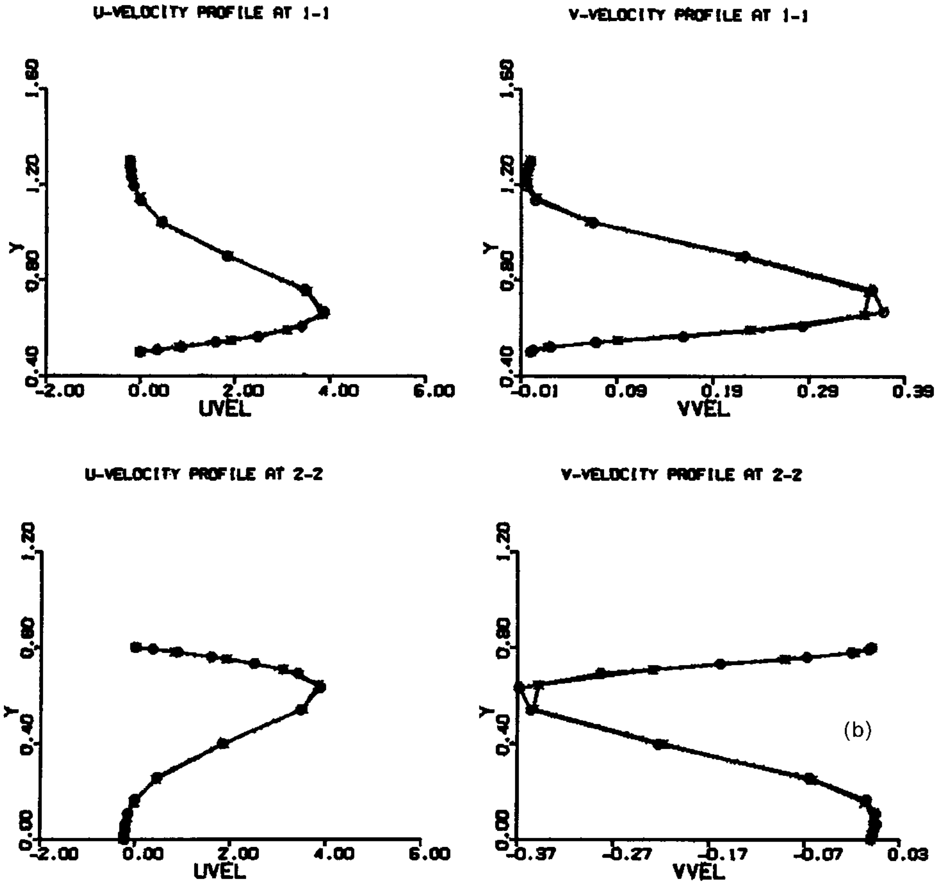

Figure 4(b). *u*- and *v*-velocity profiles at section 5 1–1 and 2–2 (see Figure 3) for the two mesh configurations with different numbers of nodes and different inlet and outlet boundary locations reattachment occurs at about 30° on the front of the cylinders and the separation point lies near 145°. Recirculating flow is trapped between cylinders which appears to be similar to cavity flows.

Figure 5(a) shows the streamlines for flow past a staggered bundle of cylinders in an equilateral triangular arrangement for $Re = 100$. Reattachment and separation points for the intermediate cylinders are seen to occur around 30° and 145°, respectively. The gaps between the cylinders enclosed by the $\psi_{\min} = 0$ and $\psi_{\max} = 1{\cdot}30$ contours indicate recirculating regions. Streamlines in regions I and II of Figure 2 are almost identical, indicating fully developed flow in these regions. A pair of elongated vortices is seen behind the last row. Figures 5(b), 5(c) and 5(d) show typical plots of isotherms, isobars and isovorticity lines for $Re = 200$. The contours plotted represent the non-dimensional quantity $\omega' = (\omega - \omega_{\min})/(\omega_{\max} - \omega_{\min})$ which range from 0 to 1, ω being pressure p, temperature θ or vorticity ζ as the case may be. The overall pattern of the contours in all the cases remains similar for different Reynolds numbers and pitch-to-diameter ratios. When dissipation is negligible, the equations governing the fields of temperature and vorticity are identical. As a consequence, the isotherms and isovorticity lines have similar patterns, as can be seen from Figures 5(b) and 5(d). The isobars in turn indicate a uniform pressure in the cavity regions and a characteristic bulge in the neighbourhood of reattachment. In Figure 5(e) streamlines and isobars are plotted together to expose the relation between the kinematics and the traction forces in the system. Near the walls of the cylinders, one can identify maxima in the pressure distribution, very near the points of reattachment. Downstream of reattachment and near the wall, the pressure drops mainly due to the inviscid effect of accelerating flow. However, beyond the hump of each cylinder, the pressure does not recover, owing to viscous effects and thus pressure drops continuously in the direction of the flow.

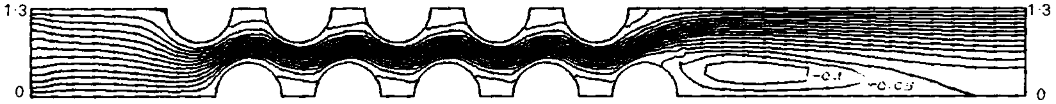

Figure 5(a). Streamlines ψ with $\Delta\psi = 0{\cdot}1$ except for the vortex region behind the last row ($\Delta\psi = 0{\cdot}05$) for the equilateral triangular arrangement in Figure 1(a) with $Re = 100$ and $P/D = 1{\cdot}5$

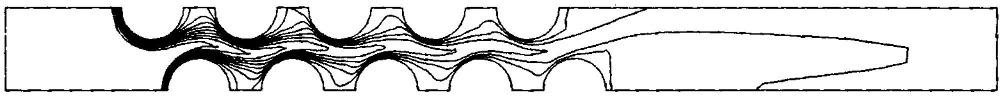

Figure 5(b). Isotherms θ with $\Delta\theta = 0{\cdot}1$ and $\theta_{\max} = 1{\cdot}0$ on cylinder surfaces for the five-row-deep bundle of cylinders in Figure 1(a); $Re = 200$, $P/D = 1{\cdot}5$ and $Pr = 0{\cdot}7$

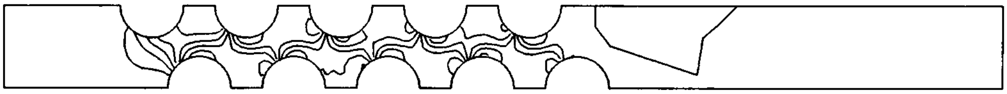

Figure 5(c). Isobars of $p' = (p - p_{\min})/(p_{\max} - p_{\min})$ with $\Delta p' = 0{\cdot}05$ for the five-row deep bundle of cylinders in Figure 1(a); $Re = 200$, $P/D = 1{\cdot}5$

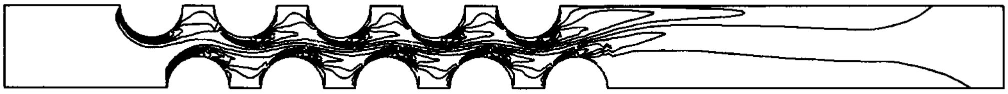

Figure 5(d). Isovorticity lines of $\zeta' = (\zeta - \zeta_{\min})/(\zeta_{\max} - \zeta_{\min})$ with $\Delta\zeta' = 0{\cdot}05$ for the five-row-deep bundle of cylinders in Figure 1(a); $Re = 200$, $P/D = 1{\cdot}5$

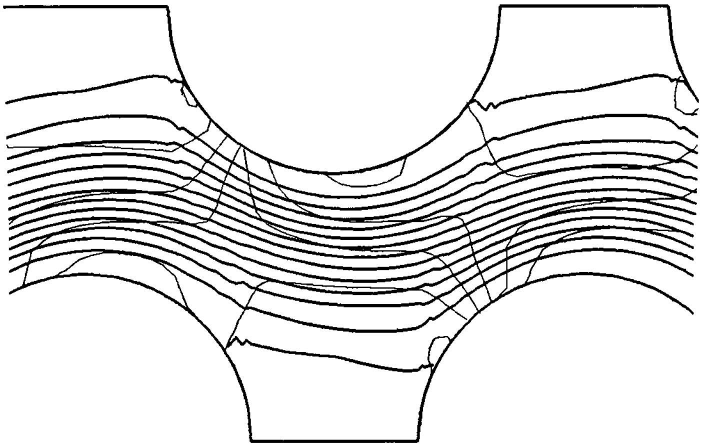

Figure 5(e). Streamlines (bold lines) and isobars (faint lines) between the third and fourth cylinders of a five-row-deep staggered bundle of cylinders; $Re = 100$, $P/D = 1{\cdot}5$

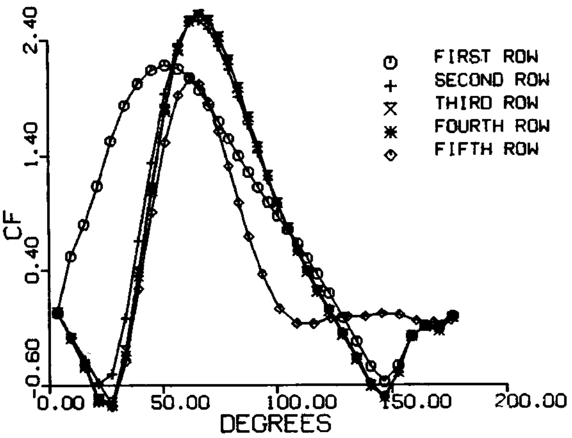

Figure 6(a). Distribution of skin friction coefficient around the five cylinders of Figure 1(a) for $Re = 200$, $P/D = 1{\cdot}5$

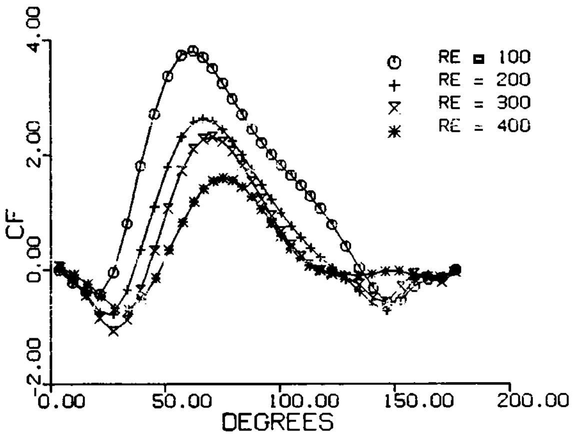

Figure 6(b). Distribution of skin friction coefficient around the bottom fourth cylinder in Figure 1(a) for different Reynolds numbers and $P/D = 1{\cdot}5$

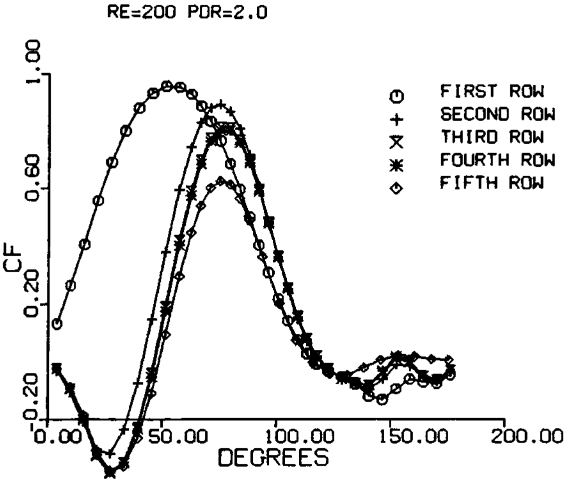

Figure 6(c). Distribution of skin friction coefficient around the five cylinders for $Re = 200$, $P/D = 2{\cdot}0$

Figures 6(a), 6(b) and 6(c) show the distribution of skin friction coefficient ($c_f = 2/(\frac{1}{2}\rho U_\infty^2)$) for a line of cylinders with the configuration shown in Figure 1(a). The point of reattachment ($c_f = 0$) is near 40° for all cylinders after the first. The point of separation ($c_f = 0$) occurs near 130°. Figure 6(b) shows the distribution of skin friction coefficient for the fourth cylinder at different values of Reynolds numbers. The point of reattachment moves from 30° to 50° and the separation point moves from 135° to 110° as the Reynolds number is increased from 100 to 400. For a particular Reynolds number, the point of reattachment and point of separation have approximately the same angular positions for all cylinders. Figure 6(c) gives the skin friction coefficient distribution around the cylinders for a pitch to diameter ratio of 2·0. Figure 6(d)

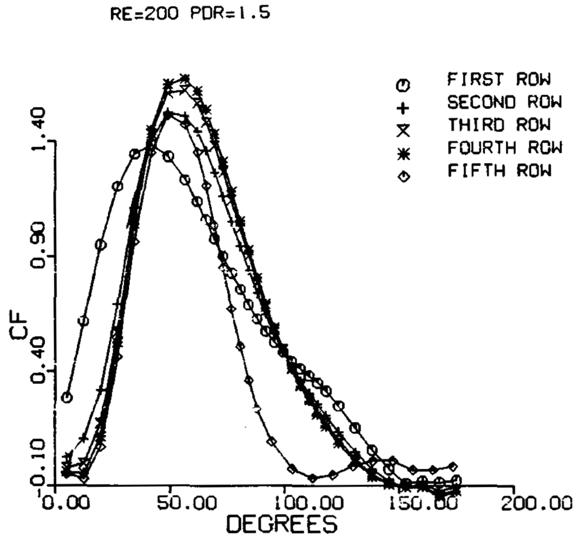

Figure 6(d). Distribution of skin friction coefficient around the five cylinders in Figure 1(c) for $Re = 200$ and $R/D = 1{\cdot}5$

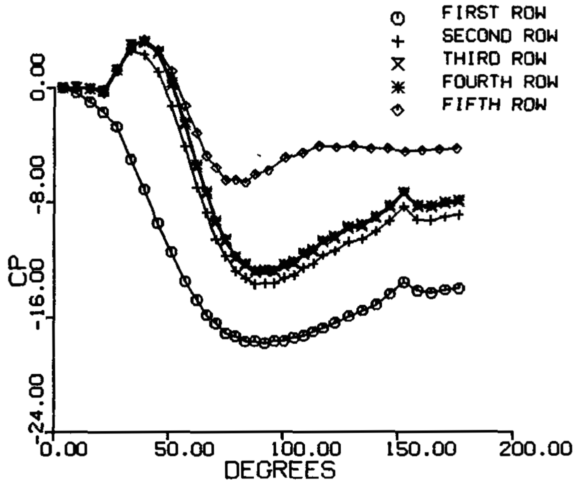

Figure 7(a). Distribution of coefficient of pressure around the five cylinders numbered in Figure 1(a) for $Re = 200$, $P/D = 1{\cdot}5$

shows the skin friction coefficient around the cylinders for the case of the staggered square arrangement of Figure 1(c).

Figure 7(a) shows the distribution of pressure coefficient ($c_p = (p - p_0)/(\frac{1}{2}\rho U_\infty^2)$) for the bottom five cylinders in the computational domain of Figure 1(a). Here p_0 is the pressure at $\phi = 0°$ on the cylinder and p is the pressure along its surface. The pressure distribution for the first row is similar to the pressure distribution for a single cylinder except that separation occurs much further downstream, at approximately $\phi = 140°$. This is verified by the fact that the point of minimum local Nusselt number and the point of minimum coefficient of skin friction occur at near $\phi = 140°$. The pressure drop from one row to the next for the middle rows is almost uniform. Pressure distributions for the third and the fourth rows are almost identical, indicating that the flows around them are dynamically similar. The distribution of pressure coefficient for the fourth cylinder at different Reynolds numbers is shown in Figure 7(b). The pressure coefficient is higher for higher Reynolds number and the pressure drop across a cylinder is higher for lower Reynolds number. Moreover, one can detect once more by the flattened portion of the distributions the fact that the

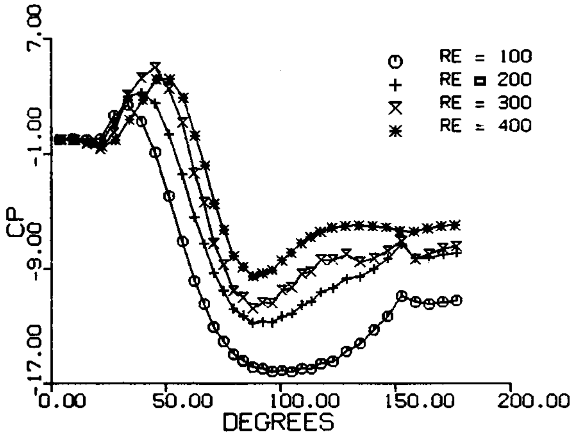

Figure 7(b). Distribution of coefficient of pressure around the fourth cylinder in Figure 1(a) for different *Re* and $P/D = 1{\cdot}5$

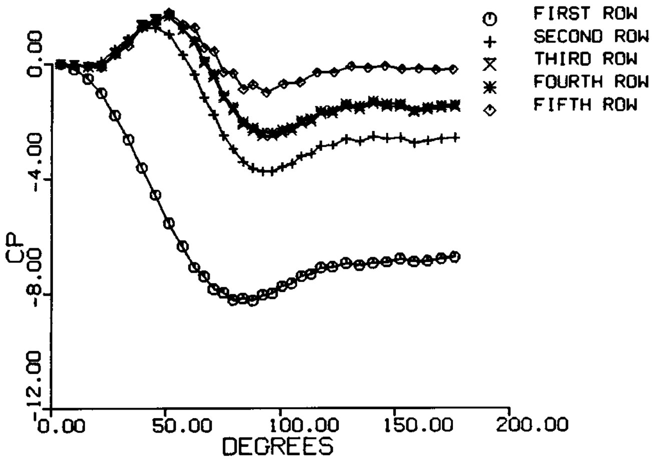

Figure 7(c). Distribution of coefficient of pressure around the five cylinders in Figure 1(a) for $Re = 200$, $P/D = 2{\cdot}0$

size of the separated region increases as the Reynolds number increases. Figure 7(c) shows the distribution of the coefficient of pressure around the cylinders for a pitch-to-diameter ratio of 2. As can be seen from Figures 7(a) and 7(c), for higher pitch-to-diameter ratio the pressure drop across a cylinder is lower. Figure 7(d) gives the pressure coefficients for the cylinders in Figure 1(c). Figure 7(e) shows a typical pressure distribution, ($c_p = (p - p_{in})/(\frac{1}{2}\rho U_\infty^2)$), where p_{in} is the stagnation pressure on the first cylinder, along the top (AB) and the bottom (CD) lines of Figure 1(a) for

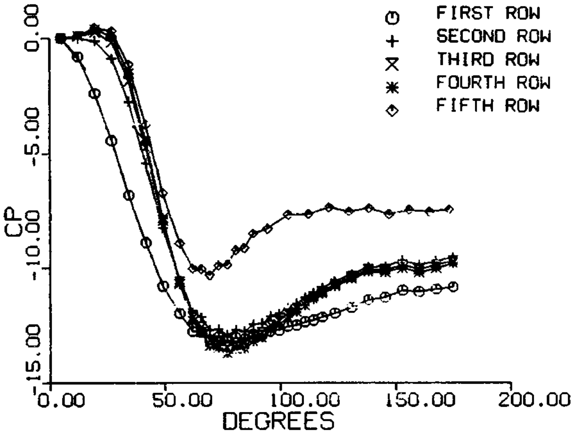

Figure 7(d). Distribution of coefficient of pressure around the five cylinders in Figure 1(c) for $Re = 200$ and $P/D = 1{\cdot}5$

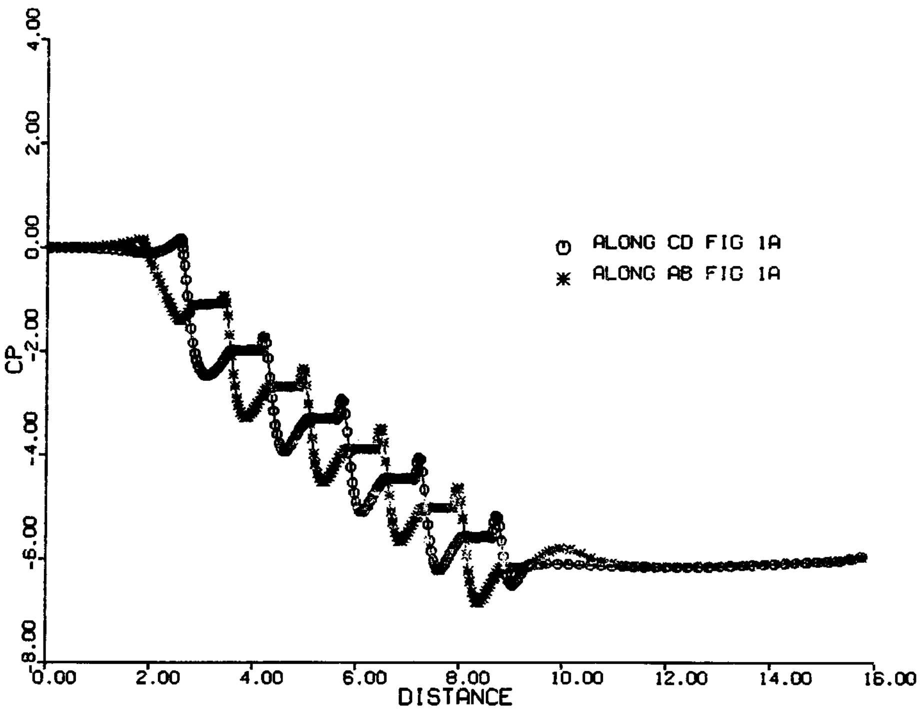

Figure 7(e). Streamwise distribution of coefficient of pressure along lines AB and CD in Figure 1(a) for $Re = 200$, $P/D = 1{\cdot}5$ and $Pr = 0{\cdot}7$

$Re = 200$ and $P/D = 1{\cdot}5$. This Figure displays most clearly the almost uniform rate of pressure drop across a row of cylinders.

Distributions of local heat transfer coefficient around the five cylinders (see Figure 1(a)) are shown in Figures 8(a), 8(b) and 8(c). The Nusselt number, Nu is based on the difference between the wall temperature and the bulk temperature along the vertical line through the centre of the cylinder under consideration. Thus

$$Nu = \frac{T_w - T_{in}}{T_w - T_b} \left. \frac{\partial \theta}{\partial r} \right|_{r=R},$$

where T_{in} is the inlet temperature and r is the radial co-ordinate.

The local Nusselt number distribution has the same form for all the cylinders except the front and the last cylinders. The local Nusselt number distribution shows only a small change for the middle rows. The maximum Nusselt number for the bottom line of cylinders in Figure 1(a)

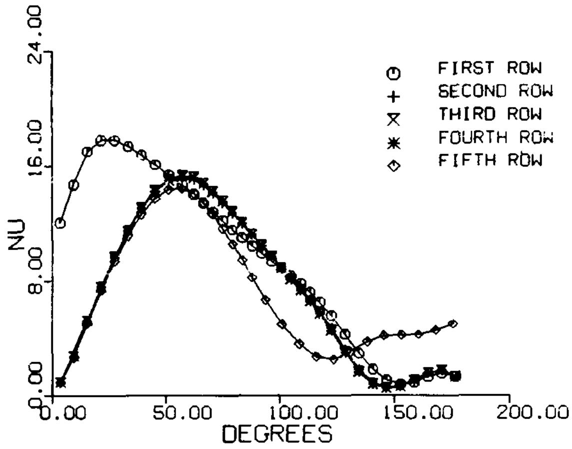

Figure 8(a). Distribution of local heat transfer coefficient around the bottom five cylinders of Figure 1(a) for $Re = 200$, $P/D = 0{\cdot}5$ and $Pr = 0{\cdot}7$

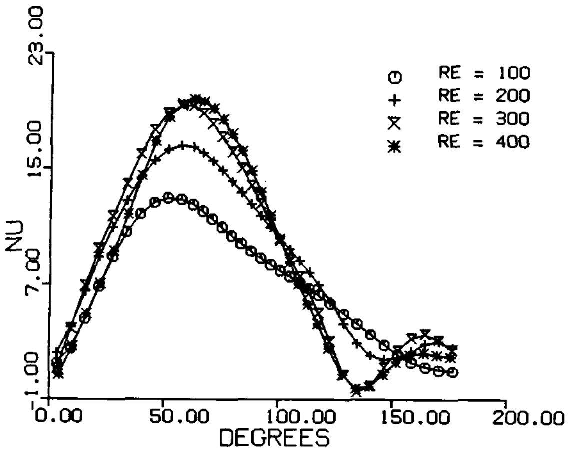

Figure 8(b). Distribution of local heat transfer coefficient around the fourth cylinder in Figure 1(a) for different Re and $P/D = 1{\cdot}5$

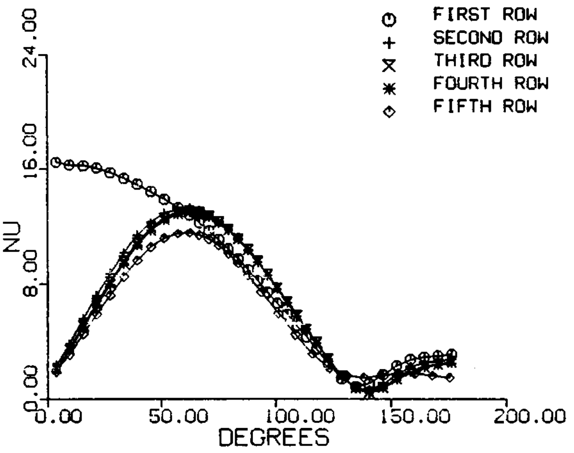

Figure 8(c). Distribution of local heat transfer coefficient around the five cylinders in Figure 1(a) for $Re = 200$, $P/D = 2{\cdot}0$ and $Pr = 0{\cdot}7$

occurs near 60°, except for the front cylinder for which the maximum occurs at near 25°. It is observed that for flow coming onto a single cylinder, the local heat transfer has a continuously decreasing slope around $\phi = 0°$. However, in the present case the flow is disturbed by the front cylinders in the adjacent columns and the local heat transfer has a positive slope at $\phi = 0°$. Pitch-to-diameter ratio and the particular arrangement of the cylinders are seen strongly to influence this behaviour. Figure 8(b) shows the local Nusselt number distribution for the fourth row bottom cylinder at different Reynolds numbers. It is seen that, although the average heat transfer coefficient increases with higher Reynolds numbers, the local heat transfer coefficient is not higher everywhere around the cylinder. This is due to the fact that the size of the separated region, where the heat transfer is low, increases with Reynolds number. Figure 8(c) gives the distribution of local Nusselt number for P/D of 2·0. From Figures 8(a) and 8(c) it can be seen that the coefficient of heat transfer decreases with the increase of pitch-to-diameter ratio. In other words more compact cylinders at these Reynolds numbers will improve heat transfer characteristics, but will lead to larger pressure drops, and therefore higher flow resistance. Figure 8(d) shows the distribution of local heat transfer coefficient around the cylinders for the staggered square arrangement.

Figure 9 shows the averaged heat transfer coefficients for a pitch-to-diameter ratio of 1·5 for the three cases of staggered bundles of cylinders. The experimental results of Bergelin *et al.*[5] and the numerical results of Antonopoulos[10] are also shown for comparison. The averaged Nusselt number is based on a log-mean temperature difference defined by

$$\Delta t_{\mathrm{lm}} = \frac{(T_{\mathrm{w}} - T_{\mathrm{in}}) - (T_{\mathrm{w}} - T_{\mathrm{out}})}{\ln[(T_{\mathrm{w}} - T_{\mathrm{in}})/(T_{\mathrm{w}} - T_{\mathrm{out}})]}.$$

The present results are in good agreement with the experimental results of Bergelin *et al.* and the numerical results of Antonopoulos.

The drag coefficients, defined as $c_{\mathrm{d}} = (p - p_{\mathrm{in}}/(\frac{1}{2}n\rho U_{\mathrm{m}}^2)$, for different Reynolds numbers are shown in Figure 10 for the case of Figure 1(a). The results of Bergelin *et al.* and Antonopoulos are shown for comparison. The present results predict slightly higher values of the drag coefficients as compared to the results of Bergelin *et al.*[5] and Antonopoulos.[10]

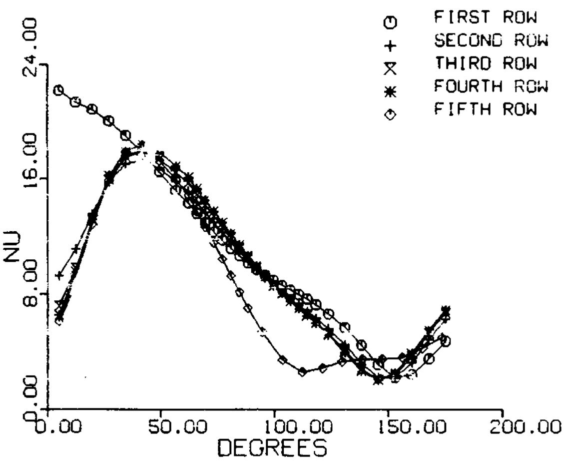

Figure 8(d). Distribution of local heat transfer coefficient around the five cylinders in Figure 1(c) for $Re = 200$, $P/D = 1{\cdot}5$ and $Pr = 0{\cdot}7$

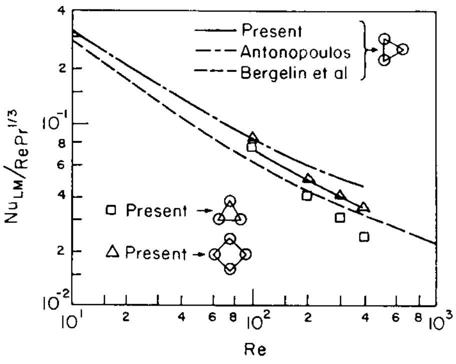

Figure 9. Comparison of averaged heat transfer coefficient with experimental and numerical results: $P/D = 1{\cdot}5$

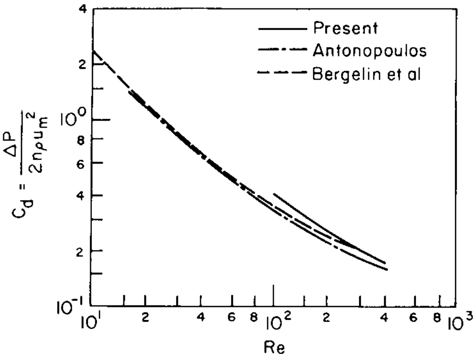

Figure 10. Drag coefficient for the five-row-deep staggered bundle of cylinders in Figure 1(b)

CONCLUSIONS

The method presented here is readily available for a parametric study, in which the geometrical parameters and the Reynolds and Prandtl numbers can be varied to provide comparative information. The method generates important integral characteristics, such as overall flow resistance or heat transfer. Detailed local distributions of heat flux, skin friction and pressure are also generated.

The local distribution of skin friction, pressure and heat transfer coefficients are consistent with the flow characteristics indicated by streamlines, velocity field vectors, isobars, isovorticity lines and isotherms. The averaged heat transfer coefficients are in good agreement with available experimental and numerical results. The coefficient of pressure is higher for higher Reynolds number, but pressure drop across a cylinder is lower for higher Reynolds number. For higher pitch-to-diameter ratio the coefficient of heat transfer and also the flow resistance are lower for a particular Reynolds number. In the range of Reynolds numbers studied, the staggered square arrangement gives a higher value of the averaged heat transfer coefficient as compared to either case of the equilateral triangular arrangements.

ACKNOWLEDGEMENTS

The support of the U.S. Department of Energy, Grant No. DE-A505-82ER12022 is gratefully acknowledged. This is a project in the programme of Dr. Oscar P. Manley, Division of Engineering, Mathematical and Geosciences of the office of Basic Energy Sciences. It is also a pleasure to acknowledge the computer time provided by the DoE on the CRAY at the University of Minnesota.

REFERENCES

1. A. Zukauskas, 'Heat transfer from tubes in cross flow', *Adv. Heat Transfer*, **8,** 93–160 (1972).
2. S. Aiba, H. Tsuchida and T. Ota, 'Heat transfer around tubes in-line tube banks', *Bulletin of the JSME*, **25,** (204), 919–926 (1982).
3. Z. Kostic and S. Oka, 'Fluid flow and convection heat transfer in boundary layer on smooth cylindrical surface of a tube in a tube bank in a crossflow', *Heat and Mass Transfer in Boundary Layers*, **1,** 451–458 (1972).
4. O. P. Bergelin, G. A. Brown, H. L. Hull and F. W. Sullivan, 'Heat transfer and fluid friction during viscous flow across bank of tubes—III. A study of tube spacing and tube size', *Trans. ASME*, **72,** 881–888 (1950).
5. O. P. Bergelin, G. A. Brown and S. C. Doberstein, 'Heat transfer and fluid friction during flow across banks of tubes–IV. A study of the transition zone between viscous and turbulent flow', *Trans. ASME*, **74,** 953–960 (1952).
6. T. VandenBerghe, M. N. Dhaubhadel, T. E. Diller and D. P. Telionis, 'Pulsating flow and heat transfer over multiple cylinders', *Proc. Symp. of DOE Conference*, Pennsylvania, Oct. 1985.
7. R. F. LeFeuvre, 'Laminar and turbulent forced convection processes through in-line tube banks', Imperial College London, Mech. Eng. Dept., *HTS/74/5*, 1973.
8. B. E. Launder and T. H. Massey, 'Numerical predictions of viscous flow and heat transfer in tube banks', *Journal of Heat Transfer*, **100,** 565–571 (1978).
9. M. Fujii, T. Fujii and T. Nagata, 'A numerical analysis of laminar flow and heat transfer of air to in-line tube bank', *Numerical Heat Transfer*, **7,** 89–102 (1984).
10. K. A. Antonopoulos, 'Heat transfer in tube assemblies under conditions of laminar axial, transverse and inclined flow', *International Journal of Heat and Fluid Flow*, **6,** 193–204 (1985).
11. M. Kawahara and H. Hirano, 'A finite element method for high Reynolds number viscous fluid flow using two step explicit scheme', *Int. j. numer. methods fluids*, **3,** 137–163 (1983).
12. P. M. Gresho, S. T. Chan, R. L. Lee and C. D. Upson, 'A modified finite element method for solving the time dependent incompressible Navier–Stokes equations', *Int. j. numer. methods fluids*, **4,** 619–640 (1984).
13. A. N. Brooks and T. J. R. Hughes, 'Streamline upwind/Petrov–Galerkin formulations for convection dominated flows with particular emphasis on the incompressible Navier–Stokes equations', *Computer Methods in Applied Mechanics and Engineering*, **32,** 199–259 (1982).
14. J. P. Benque, P. Esposito and G. Labadie, 'New decomposition finite element methods for the Stokes problem and the Navier–Stokes equations', *Proc. of the Third International Conference*, Seattle, August 1983.

15. M. N. Dhaubhadel, J. N. Reddy and D. P. Telionis, 'Penalty finite-element analysis of coupled fluid flow and heat transfer for in-line bundle of cylinders in cross flow', *Int. J. Nonlinear Mechanics*, **21**, (5), 361–373 (1986).
16. J. N. Reddy, 'On penalty function methods in the finite element analysis of flow problems', *Int. j. numer. methods fluids*, **2**, 151–171 (1982).
17. J. N. Reddy, 'Penalty-finite-element analysis of 3-D Navier–Stokes equations', *Computer Methods in Applied Mechanics and Engineering*, **35**, 87–106 (1982).
18. J. N. Reddy, 'Penalty-finite element methods in conduction and convection heat transfer', in R. W. Lewis, K. Morgan and B. A. Schrefler (eds), *Numerical Methods in Heat Transfer, Vol. II*, Wiley, Chichester, 1983, pp. 145–177.
19. J. N. Reddy, *Applied Functional Analysis and Variational Methods in Engineering*, McGraw-Hill, New York, 1986.
20. J. N. Reddy, *An Introduction to the Finite Element Method*, McGraw-Hill, New York, 1984.